A Novel Hybrid Analytical Model of Active Magnetic Bearing Considering Rotor Eccentricity and Local Saturation Effect

Cao, Zhi; Huang, Yunkai; Guo, Baocheng; Peng, Fei; Dong, J. N.; Hemeida, Ahmed

DOI
10.1109/TIE.2021.3102396

Publication date
2022

Document Version
Final published version

Published in
IEEE Transactions on Industrial Electronics

A Novel Hybrid Analytical Model of Active Magnetic Bearing Considering Rotor Eccentricity and Local Saturation Effect

Zhi Cao, Yunkai Huang, Baocheng Guo, *Member, IEEE*, Fei Peng, *Member, IEEE*, Jianning Dong, *Member, IEEE*, and Ahmed Hemeida, *Member, IEEE*

***Abstract*—To facilitate the active magnetic bearing (AMB) design and analysis, an accurate and fast model that considers both rotor eccentricity and the saturation effect is necessary. In this article, a novel hybrid analytical model (HAM) for effective calculation of the magnetic field of the AMB is proposed. Eccentricity and local saturation are considered in the proposed HAM. In the proposed HAM, the stator and rotor are modeled by elementary subdomains (ESDs) and the air-gap is modeled by magnetic equivalent circuit (MEC). Direct coupling between the solutions in the ESD regions with MEC completes the whole model matrices. Compared to the existing literature, the proposed model considers both the rotor eccentricity and material nonlinearity. The effectiveness and accuracy of the proposed HAM are validated by both the finite element model and experimental results. The results show that the proposed HAM can accurately predict the magnetic quantities of the AMB.**

***Index Terms*—Active magnetic bearing (AMB), analytical model, hybrid model, magnetic equivalent circuit (MEC), material nonlinearity, rotor eccentricity, saturation, subdomain method.**

Nomenclature

AMB	Active magnetic bearing.
HAM	Hybrid analytical model.
SD	Subdomain.
ESD	Elementary subdomain.
MEC	Magnetic equivalent circuit.
FEM	Finite-element model.
AM	Analytical model.
BC	Boundary condition.

Manuscript received January 11, 2021; revised April 12, 2021 and June 15, 2021; accepted July 23, 2021. Date of publication August 10, 2021; date of current version February 9, 2022. This work was supported in part by the National Natural Science Foundation of China under Grant 51777034, Grant 51707037, and Grant 51907027. *(Corresponding author: Yunkai Huang.)*

Zhi Cao, Yunkai Huang, and Fei Peng are with the School of Electrical Engineering, Southeast University, Nanjing 210096, China (e-mail: caozhi@seu.edu.cn; huangyk@seu.edu.cn; pengfei@seu.edu.cn).

Baocheng Guo is with the School of Electrical and Automation Engineering, Nanjing Normal University, Nanjing 210023, China (e-mail: bc.guo@njnu.edu.cn).

Jianning Dong is with the Delft University of Technology, 2628 CD, Delft, The Netherlands (e-mail: J.Dong-4@tudelft.nl).

Ahmed Hemeida is with the Electrical Power and Engineering Department, Cairo University, Cairo 12613, Egypt (e-mail: a.hemeida@eng.cu.edu.eg).

Color versions of one or more figures in this article are available at https://doi.org/10.1109/TIE.2021.3102396.

Digital Object Identifier 10.1109/TIE.2021.3102396

I. Introduction

ACTIVE magnetic bearings (AMBs), compared with conventional mechanical bearings, are gaining more and more attention in various high-speed industrial applications. It has attractive features such as contactless operation, no lubrication needed, no mechanical wear, and ability to actively control rotor dynamics [1].

Normally, the linear AMB model characterizing the relation of magnetic force versus current and displacement is used for the controller design and simulation [1]–[3]. However, the AMB system is highly nonlinear, and linear model is not accurate and its parameters have to vary with the change of the operating point. In some cases, such as starting and load variation, the AMB system has to go through eccentric and saturated conditions. In such case, the linear model will result in inaccurate results. Thus, better model of AMB with high accuracy in the full operation range and low calculation burden is required. FEM is a popular and powerful tool for accurately predicting the electromagnetic performance for many different actuators [4]. However, FEM has the obvious disadvantages of time and computational consumption.

Compared with FEM, the analytical models (AMs) require lower CPU resources and can obtain solutions with acceptable accuracy. Different AMs have been developed to predict the magnetic field for different electrical machines. Therein the subdomain (SD) method uses the harmonic model technique in all subdomains (e.g., air-gap, stator/rotor slots, and magnets) assuming that the infinite magnetic permeability in the ferromagnetic materials [5], [6]. However, these models are only valid in the linear part of the magnetization curve.

Recently, an elegant superposition principle formulation for the SD model is developed in parallel by Dubas and Boughrara [7] and Devillers [8] to the include global saturation. This technique is further extended to an elementary subdomain level for the full prediction of the magnetic field in the rotating electrical machines with the local saturation effect by the Newton–Raphson iterative algorithm in [9]. However, these SD models are only featured with solutions derived for perfect

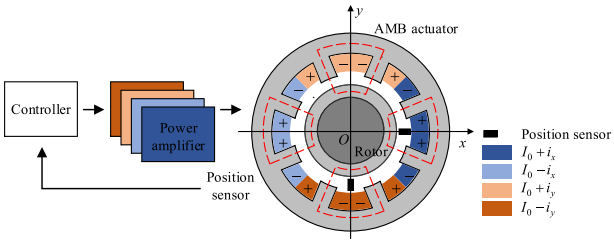

Fig. 1. Schematic diagram of a 2-DOF AMB system.

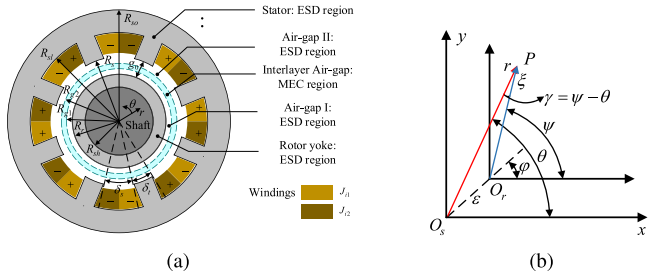

Fig. 2. (a) Illustrative representation of a heteropolar AMB. (b) Coordinate relationships of the fixed and moving coordinates.

annular domains, which are not applicable for the nonannular air gap domain under the rotor eccentricity.

To solve eccentricity problems, two approaches are widely used. The first one is the perturbation method [5], [6], which considers the first-order term by Taylor series expansion, and the other one adopts the superposition method [10]–[12]. The original eccentric state is first divided into several concentric states, then is superposed. The perturbation method is theoretically complex and can only achieve accurate solutions in a small range of eccentricity, while the superposition method requires longer computation time than perturbation method, and it is expected to have a nonnegligible error at the boundaries between sections [13].

Most, if not all, previous studies [5]–[12] are not able to provide a simple, fast, and accurate approach to consider both eccentricity and local saturation. To facilitate the AMB design and analysis, a fast AM that takes into account both rotor eccentricity and the saturation effects is preferable. Inspired by the methodology in [9], [14], and [15], a novel hybrid analytical model (HAM)-based on the ESD technique and MEC is presented for the AMB design and analysis in this article. To make up for the deficiency of the ESD model in dealing with the eccentric problem, an MEC model region in the middle of the air gap is introduced to model the nonannular region under the rotor eccentricity. Furthermore, the direct coupling boundary conditions between ESD regions and the MEC region are derived based on the air-gap region division technique.

This article is organized as follows. The ESD technique can consider the local nonlinear behavior of the material in the stator and rotor. The MEC is used to model the uneven air-gap under rotor eccentricity and directly coupled with ESDs. Thus, the model matrices are assembled and solved by the Newton–Raphson method. All results obtained with HAM are compared with and validated by 2-D FEM. Finally, two-degree-of-freedom 2-DoF AMB suspension experiment is designed to further verify the proposed model.

II. Introduction and Parameters of the Studied AMB

A typical 2-DOF radial AMB system is shown in Fig. 1. This system includes an AMB actuator, a rotor, position sensors, a controller, and power amplifiers. The rotor is kept at the center point by controlling the currents in the coils. The coils are grouped into four sets (distinguished by color in Fig. 1) in the x and y directions. The expressions of currents in the coils are given in Fig. 1, where I_0 is the bias current, and i_x, i_y are the control currents. The geometric parameters of the radial heteropolar AMB are depicted in Fig. 2(a) in detail: the rotor shaft radius R_{sh}, the rotor yoke radius R_r, the stator bore radius R_s, the stator slot bottom radius R_{sl}, the stator outer radius R_{so}, the stator slot span angle δ_s, the stator tooth width angle δ_t, and the nominal air-gap length g_0. The sign $+/-$ in the figures denotes the direction of the currents in the coils. A maximum of 50% eccentricity is considered in this article due to the limit of back-up bearings. The specifications of the studied AMB in this article are listed in Table I.

TABLE I
Specifications of a Heteropolar AMB

Parameter	Symbol	Value
rotor shaft radius	R_{sh}	0.020 m
rotor yoke radius	R_r	0.030 m
stator bore radius	R_s	0.0304 m
stator slot bottom radius	R_{sl}	0.0394 m
stator outer radius	R_{so}	0.0494 m
stator slot span angle	δ_s	0.4550 rad
stator tooth width angle	δ_t	0.3304 rad
stack length	L_z	0.070 m
turns of winding	N_c	25
bias current	I_0	3 A
nominal air-gap length	g_0	0.0004 m

III. Proposed Hybrid Analytical Model for Full Prediction of the Magnetic Field

To achieve effective analysis of the magnetic field of the AMB, a hybrid analytical model is presented in this section. This model takes into account rotor eccentricity and local nonlinearity of the iron core. It can predict the magnetic field distribution of the AMB in all regions.

To simplify the analysis, the following assumptions are made.

1) The geometry is 2-D in polar coordinates.
2) The stator slots have radial sides.
3) The end effect is ignored due to very short ending winding of the concentrated winding (i.e., the magnetic variables are independent of z).
4) The magnetic vector potential and current density have only z-axis components.
5) The ESDs are considered as isotropic regions.

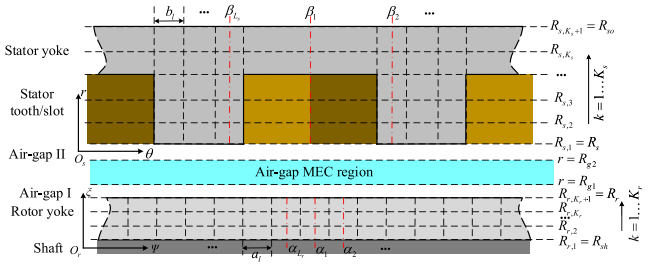

Fig. 3. Schematic diagram of ESD mesh generation in the stator and the rotor.

A. Coordinate Systems and Region Division

The following two coordinate systems are depicted in Fig. 2 (b):

1) O_s–r–θ coordinate system fixed to the center of the stator;
2) O_r–ξ–ψ coordinate system which is attached to the center of the rotor.

The relative position of the rotor with respect to the stator is characterized by eccentricity distance ε and angle φ. The coordinate transformations of two reference frames can be found in [16].

The hybrid analytical model combines the 2-D ESD technique and the nodal-based MEC by strong coupling boundary conditions. Since the boundary conditions between non-periodic subdomains (e.g., stator slots and teeth) and the MEC region are complicated to derive, the air-gap region is divided into three layers modeled by the ESD and MEC, respectively. Thus, the derivation of the boundary conditions between periodic subdomains and the MEC region is simpler. The complete division of the regions is shown in Fig. 2(a). The stator and air-gap I are modeled by ESD in O_s–r–θ system while the rotor and air-gap II are modeled by ESD in O_r–ξ–ψ system. Only the inter layer in the middle of the air-gap is modeled with MEC in O_s–r–θ coordinate system to address the problem of rotor eccentricity.

B. Solutions in the ESD Regions

The ESD modeling applies the general solutions of magnetostatic Maxwell's equations using the superposition principle in [7], [8], and [17]. It is able to take into account the finite relative permeability of the ferromagnetic material. The rotor and stator are subdivided into multiple smaller sector regions in radial and circumferential directions as shown in Fig. 3. For convenience, only partial unrolled stator and rotor are displayed in Fig. 3. In general, the meshing in the ESD regions can be nonuniform. The meshing is performed such that the material boundaries of the geometry are coinciding with the edges of the ESDs. As a result, L_s sections in the circumferential direction and K_s layers are obtained for the stator region while L_r sections in the circumferential direction and K_r layers are obtained for the rotor region.

Afterward, the air-gap is divided into three layers characterized by the geometric parameters R_s, R_{g1}, R_{g2}, and R_r in Fig. 3. As a result, one layer is concentric with the stator, one layer is concentric with the rotor, the inter layer is modeled by MEC.

The general solutions of each ESD are formulated in terms of magnetic vector potential.

1) General Solutions in the Air-Gap Regions I and II: The air-gap regions I and II are periodic annular domains, the solutions of Laplace's equations in these two regions are given as

$$\begin{aligned} A_z^{\mathrm{I}} &= A_{10}^{\mathrm{I}} + A_{20}^{\mathrm{I}} \ln(\xi) \\ &\quad + \sum_{n=1}^{N} \left(A_{1n}^{\mathrm{I}} \left(\frac{\xi}{R_{g1}} \right)^n + A_{2n}^{\mathrm{I}} \left(\frac{R_r}{\xi} \right)^n \right) \sin(n\psi) \\ &\quad + \sum_{n=1}^{N} \left(A_{3n}^{\mathrm{I}} \left(\frac{\xi}{R_{g1}} \right)^n + A_{4n}^{\mathrm{I}} \left(\frac{R_r}{\xi} \right)^n \right) \cos(n\psi) \end{aligned} \tag{1}$$

$$\begin{aligned} A_z^{\mathrm{II}} &= A_{10}^{\mathrm{II}} + A_{20}^{\mathrm{II}} \ln(r) \\ &\quad + \sum_{n=1}^{N} \left(A_{1n}^{\mathrm{II}} \left(\frac{r}{R_s} \right)^n + A_{2n}^{\mathrm{I}} \left(\frac{R_{g2}}{r} \right)^n \right) \sin(n\theta) \\ &\quad + \sum_{n=1}^{N} \left(A_{3n}^{\mathrm{II}} \left(\frac{r}{R_s} \right)^n + A_{4n}^{\mathrm{II}} \left(\frac{R_{g2}}{r} \right)^n \right) \cos(n\theta) \end{aligned} \tag{2}$$

where $\{A_{10}^{\mathrm{I}}\ A_{20}^{\mathrm{I}}\ A_{1n}^{\mathrm{I}}\ A_{2n}^{\mathrm{II}}\ A_{3n}^{\mathrm{I}}\ A_{4n}^{\mathrm{I}}\}$ and $\{A_{10}^{\mathrm{II}}\ A_{20}^{\mathrm{II}}\ \ A_{1n}^{\mathrm{II}}\ A_{2n}^{\mathrm{II}}\ A_{3n}^{\mathrm{II}}\ A_{4n}^{\mathrm{II}}\}$ are the integration constants in Regions I and II, respectively, N is the maximum number of harmonics considered in the air-gap regions.

2) General Solutions in the Rotor Regions: Each ESD in the rotor regions is characterized by its inner radii $R_{r,k}$ and outer radii $R_{r,k+1}$, position angle α_l, opening width a_l, and magnetic reluctivity $v_r^{k,l}$. The general solutions of these ESDs can be expressed as

$$\begin{aligned} A_{zr}^{k,l} &= B_1^{k,l} + B_2^{k,l} \ln(\xi) \\ &\quad + \sum_{v=1}^{V_r} \left(B_{3v}^{k,l} \left(\frac{\xi}{R_{r,k+1}} \right)^{v_{rl}} + B_{4v}^{k,l} \left(\frac{\xi}{R_{r,k}} \right)^{-v_{rl}} \right) \\ &\quad \times \cos\left(v_{rl} \left(\psi - \frac{\alpha_l}{2} + a_l \right) \right) \\ &\quad + \sum_{w=1}^{W_r} \begin{pmatrix} +B_{5w}^{k,l} \sinh\left(\lambda_{rk} \left(\psi - \frac{\alpha_l}{2} + a_l \right) \right) \\ +B_{6w}^{k,l} \sinh\left(\lambda_{rk} \left(\psi - \frac{\alpha_l}{2} - a_l \right) \right) \end{pmatrix} \frac{\sin\left(\lambda_{rk} \ln\left(\frac{\xi}{R_{r,k}} \right) \right)}{\sinh(\lambda_{rk} a_l)} \end{aligned} \tag{3}$$

where $v_{rl} = v\pi/a_l$, $\lambda_{rk} = w\pi/\ln(R_{r,k+1}/R_{r,k})$, and $\{B_1^{k,l}\ B_2^{k,l}\ B_{3v}^{k,l}\ B_{4v}^{k,l}\ B_{5w}^{k,l}\ B_{6w}^{k,l}\}$ are the integration constants in the rotor ESD regions, $V_r = W_r$ is the maximum number of harmonics considered in the rotor ESDs.

3) General Solutions in the Stator Regions: Each ESD in the rotor regions is characterized by its inner radii $R_{s,k}$ and outer radii $R_{s,k+1}$, position angle β_l, opening width b_l, and magnetic reluctivity $v_s^{k,l}$. The general solutions of these ESDs of the stator

can be expressed as

$$A_{zs}^{k,l} = C_1^{k,l} + C_2^{k,l}\ln(r) + \sum_{v=1}^{V_s}\left(C_{3v}^{k,l}\left(\frac{r}{R_{s,k+1}}\right)^{v_{sl}} + C_{4v}^{k,l}\left(\frac{r}{R_{s,k}}\right)^{-v_{sl}}\right) \times \cos\left(v_{sl}(\theta - \frac{\beta_l}{2} + b_l)\right) + \sum_{w=1}^{W_s}\left(\begin{array}{l} +C_{5w}^{k,l}\sinh\left(\lambda_{sk}(\theta - \frac{\beta_l}{2} + b_l)\right) \\ +C_{6w}^{k,l}\sinh\left(\lambda_{sk}(\theta - \frac{\beta_l}{2} - b_l)\right)\end{array}\right)\frac{\sin\left(\lambda_{sk}\ln(\frac{r}{R_{s,k}})\right)}{\sinh(\lambda_{sk}b_l)} + A_{ps}^{k,l} \tag{4}$$

where $v_{sl} = v\pi/b_l$, $\lambda_{sk} = w\pi/\ln(R_{s,k+1}/R_{s,k})$, and $\{C_1^{k,l}\ C_2^{k,l}\ C_{3v}^{k,l}\ C_{4v}^{k,l}\ C_{5w}^{k,l}\ C_{6w}^{k,l}\}$ are the integration constants in the stator ESD regions, $V_s = W_s$ is the maximum number of harmonics considered in the stator ESDs, $A_{ps}^{k,l}$ is the particular solution in the slot ESD regions, which is given as [8]

$$A_{ps}^{k,l} = -\frac{1}{4}\mu_0 J_{i0} r^2 + \frac{\mu_0 J_{iv} r^2}{{v_{sl}}^2 - 4}\cos\left(v_{sl}(\theta - \frac{\beta_l}{2} + b_l)\right) \tag{5}$$

$$J_{i0} = \frac{J_{i1} + J_{i2}}{2} \tag{6}$$

$$J_{iv} = \frac{2}{v\pi}\left(J_{i1} + (-1)^v J_{i2}\right)\sin\left(\frac{v\pi}{2}\right) \tag{7}$$

with the current densities J_{i1} and J_{i2} in the ith slot shown in Fig. 2(a).

Then the radial and tangential components of flux density can be obtained from the vector potential distribution by

$$B_r = \frac{1}{r}\frac{\partial A}{\partial \theta} \quad \text{or} \quad B_\xi = \frac{1}{\xi}\frac{\partial A}{\partial \psi} \tag{8}$$

$$B_\theta = -\frac{\partial A}{\partial r} \quad \text{or} \quad B_\psi = -\frac{\partial A}{\partial \xi}. \tag{9}$$

C. Solutions in the MEC Regions

Since it is hard to give the exact analytical solutions under rotor eccentricity, the MEC technique is used to model the uneven air-gap under rotor eccentricity and to directly couple the nonconcentric stator and rotor regions.

The interlayer MEC region in the air-gap is meshed into circular sector elements in O_s–r–θ coordinate system as shown in Fig. 4. The magnetostatic problem in the MEC region is described using scalar potential. Two layers of potential nodes in the radial direction and L_{mec} sections in the circumferential direction in total are set for the MEC region. A potential node is defined at the geometrical center of each MEC element, and each MEC element is characterized by reluctance in $\pm r$ and $\pm\theta$ directions [18]

$$R_{mr}^{k,l} = \frac{1}{\mu_0 L_z \Delta\theta}\ln\left(\frac{R_{g2} - (2-k)\Delta r_l}{R_{g2} - (3-k)\Delta r_l}\right) \tag{10}$$

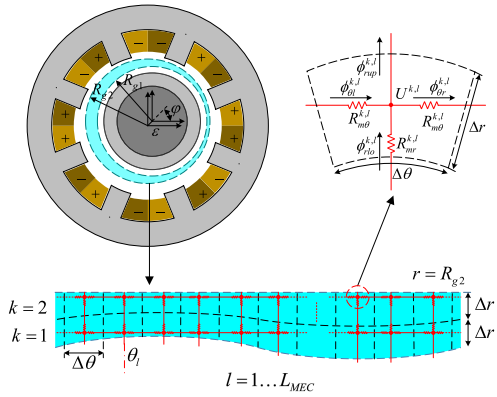

Fig. 4. Schematic graphs of the meshed MEC region and the mesh elements.

$$R_{m\theta}^{k,l} = \frac{\Delta\theta}{2\mu_0 L_z \ln\frac{R_{g2}-(2-k)\Delta r_l}{R_{g2}-(3-k)\Delta r_l}} \quad k = 1, 2 \text{ and } l = 1, \ldots, L_{mec} \tag{11}$$

where L_z is the stack length of the AMB, $\Delta\theta = 2\pi/L_{mec}$ and $\Delta r_l = g_{mec}/2$ are illustrated in Fig. 3, representing the angle in the θ direction and the length in the r direction of each MEC element, respectively. g_{mec} is the length of inter layer air-gap, and it can be written as under rotor eccentricity [16]

$$g_{mec} = g_{0mec} - \varepsilon\cos(\theta - \varphi) \tag{12}$$

where g_{0mec} is the interlayer air-gap length without rotor eccentricity. As a result, the reluctances in (10) and (11) of MEC elements vary with the rotor position.

According to the magnetic equivalence of Kirchhoff's current law applied to each MEC element, the magnetic flux going into each potential node should equal to the magnetic flux going out, namely

$$\phi_{rlo}^{k,l} - \phi_{rup}^{k,l} + \phi_{\theta l}^{k,l} - \phi_{\theta r}^{k,l} = 0 \tag{13}$$

where the magnetic flux inside each MEC element is calculated by its potential and reluctances as well as surroundings. The expressions are given in [18], and hence, are not repeated here.

Then the radial and tangential components of flux density in the MEC region shown in Fig. 3 can be obtained by

$$B_r^l = \frac{U^{1,l} - U^{2,l}}{(R_{mr}^{1,l} + R_{mr}^{2,l})S_{rl}} \tag{14}$$

$$B_\theta^{k,l} = \frac{\phi_{\theta l}^{k,l} + \phi_{\theta r}^{k,l}}{2S_{\theta l}} \tag{15}$$

where $S_{rl} = L_z(R_{g2} - \Delta r_l)\Delta\theta$ and $S_{\theta l} = L_z\Delta r_l$ are the sectional areas of the flux flow in the radial and circumferential directions of the MEC element.

D. Boundary Conditions (BCs)

After obtaining the expressions of the magnetic field inside the ESD and MEC regions, the boundary conditions are defined to obtain the unknown coefficients of the expressions. The

TABLE II
BOUNDARY CONDITIONS INSIDE ESD REGIONS

Description	Expressions
BCs bewteen air-gap I and rotor	$A_z^{\mathrm{I}}\big\vert_{\xi=R_r} = A_{zr}^{Kr,l}\big\vert_{\xi=R_r}$ $H_\psi^{\mathrm{I}}\big\vert_{\xi=R_r} = H_{\psi r}^{Kr,l}\big\vert_{\xi=R_r}$
BCs bewteen ESDs inside rotor	$A_{zr}^{k,l}\big\vert_{\xi=R_{r,k}} = A_{zr}^{k+1,l}\big\vert_{\xi=R_{r,k}}, k=1...K_{r-1}$ $H_{\psi r}^{k,l}\big\vert_{\xi=R_{r,k}} = H_{\psi r}^{k+1,l}\big\vert_{\xi=R_{r,k}}, k=1...K_{r-1}$ $A_{zr}^{k,l}\big\vert_{\psi=\alpha_l+\frac{a_l}{2}} = A_{zr}^{k,l+1}\big\vert_{\psi=\alpha_{l+1}-\frac{a_{l+1}}{2}}, l=1...L_r$ $H_{\xi r}^{k,l}\big\vert_{\psi=\alpha_l+\frac{a_l}{2}} = H_{\xi r}^{k,l+1}\big\vert_{\psi=\alpha_{l+1}-\frac{a_{l+1}}{2}}, l=1...L_r$
BCs bewteen air-gap II and stator	$A_z^{\mathrm{II}}\vert_{r=R_s} = A_{zS}^{1,l}\vert_{r=R_s}$ $H_\theta^{\mathrm{II}}\vert_{r=R_s} = H_{\theta s}^{1,l}\vert_{r=R_s}$
BCs bewteen ESDs inside stator	$A_{zs}^{k,l}\big\vert_{r=R_{s,k}} = A_{zs}^{k+1,l}\big\vert_{r=R_{s,k}}, k=1...K_{s-1}$ $H_{\theta s}^{k,l}\big\vert_{r=R_{s,k}} = H_{\theta s}^{k+1,l}\big\vert_{r=R_{s,k}}, k=1...K_{s-1}$ $A_{zs}^{k,l}\big\vert_{\theta=\beta_l+\frac{b_l}{2}} = A_{zs}^{k,l+1}\big\vert_{\theta=\beta_{l+1}-\frac{b_{l+1}}{2}}, l=1...L_s$ $H_{rs}^{k,l}\big\vert_{\theta=\beta_l+\frac{b_l}{2}} = H_{rs}^{k,l+1}\big\vert_{\theta=\beta_{l+1}-\frac{b_{l+1}}{2}}, l=1...L_s$
BCs at $\xi = R_{sh}$ BCs at $r = R_{so}$	$A_{zr}^{1,l}=0$ $A_{zs}^{K_s,l}=0$

conditions applied between two adjacent regions are based on continuity.

1) Boundary Conditions Inside ESD Regions: The boundary conditions inside the ESD regions are based on the continuity of the vector potentials and tangential component of magnetic field strength between two adjacent ESD regions. The derivation of the ESD boundary conditions are elaborated in [9], and they are summarized here in Table II.

2) Boundary Conditions Between ESD and MEC Regions: Between the ESD and MEC regions, the continuity of magnetic field has to be guaranteed, i.e., normal flux density and the tangential magnetic field strength in both the spatial frequency and space domains are consistent on the region boundaries. According to the geometric relationship at the boundary surface, the BCs between ESD regions and MEC region can be expressed as

$$H_\theta^{MEC}\big\vert_{r=R_{g2}} = H_\theta^{\mathrm{II}}\big\vert_{r=R_{g2}} \tag{16}$$

$$B_r^{MEC}\big\vert_{r=R_{g2}} = B_r^{\mathrm{II}}\big\vert_{r=R_{g2}} \tag{17}$$

$$H_\theta^{MEC}\cos\gamma - H_r^{MEC}\sin\gamma\big\vert_{r=R_{g1}} = H_\psi^{\mathrm{I}}\big\vert_{\xi=R_{g1}} \tag{18}$$

$$B_r^{MEC}\big\vert_{r=R_{g1}} = B_\xi^{\mathrm{I}}\cos\gamma - B_\psi^{\mathrm{I}}\sin\gamma\big\vert_{\xi=R_{g1}} \tag{19}$$

with detailed development of (18) and (19) provided in the Appendix.

Collecting the boundary conditions in Table II and (16) to (19) results in the total matrix equations as follows:

$$\mathbf{M}(\mathbf{X})\mathbf{X} = \mathbf{Y} \tag{20}$$

with

$$\mathbf{M}=\begin{bmatrix}
\mathbf{M_{11}} & \mathbf{0} & \mathbf{M_{13}} & \mathbf{0} & \mathbf{0} & \mathbf{0}\\
\mathbf{0} & \mathbf{0} & \mathbf{M_{23}} & \mathbf{0} & \mathbf{0} & \mathbf{0}\\
\mathbf{0} & \mathbf{M_{32}} & \mathbf{O} & \mathbf{M_{34}} & \mathbf{0} & \mathbf{0}\\
\mathbf{0} & \mathbf{0} & \mathbf{0} & \mathbf{M_{44}} & \mathbf{0} & \mathbf{0}\\
\mathbf{M_{51}} & \mathbf{0} & \mathbf{0} & \mathbf{0} & \mathbf{M_{55}} & \mathbf{0}\\
\mathbf{0} & \mathbf{M_{62}} & \mathbf{0} & \mathbf{0} & \mathbf{0} & \mathbf{M_{66}}\\
\mathbf{M_{71}} & \mathbf{M_{72}} & \mathbf{0} & \mathbf{0} & \mathbf{M_{75}} & \mathbf{M_{76}}\\
\mathbf{M_{81}} & \mathbf{0} & \mathbf{M_{83}}\,(\mathbf{B_{rotor}}) & \mathbf{0} & \mathbf{0} & \mathbf{0}\\
\mathbf{0} & \mathbf{0} & \mathbf{M_{93}}\,(\mathbf{B_{rotor}}) & \mathbf{0} & \mathbf{0} & \mathbf{0}\\
\mathbf{0} & \mathbf{M_{102}} & \mathbf{0} & \mathbf{M_{104}}\,(\mathbf{C_{stator}}) & \mathbf{0} & \mathbf{0}\\
\mathbf{0} & \mathbf{0} & \mathbf{0} & \mathbf{M_{114}}\,(\mathbf{C_{stator}}) & \mathbf{0} & \mathbf{0}
\end{bmatrix} \tag{21}$$

$$\mathbf{X} = \begin{bmatrix}\mathbf{A_{agI}}\ \mathbf{A_{agII}}\ \mathbf{B_{rotor}}\ \mathbf{C_{stator}}\ \mathbf{U_1}\ \mathbf{U_2}\end{bmatrix}^{\mathrm{T}} \tag{22}$$

$$\mathbf{Y} = \begin{bmatrix}\mathbf{0}\ \mathbf{0}\ \mathbf{Y_3}\ \mathbf{Y_4}\ \mathbf{0}\ \mathbf{Y_6}\ \mathbf{0}\ \mathbf{0}\ \mathbf{0}\ \mathbf{Y_{10}}\ \mathbf{Y_{11}}\end{bmatrix}^{\mathrm{T}} \tag{23}$$

$$\mathbf{A_{agI}} = \begin{bmatrix}A_{10}^{\mathrm{I}}\ A_{20}^{\mathrm{I}}\ A_{11}^{\mathrm{I}}\ \cdots\ A_{4N}^{\mathrm{I}}\end{bmatrix}^{\mathrm{T}} \in \Re^{2+4N} \tag{24}$$

$$\mathbf{A_{agII}} = \begin{bmatrix}A_{10}^{\mathrm{II}}\ A_{20}^{\mathrm{II}}\ A_{11}^{\mathrm{II}}\ \cdots\ A_{4N}^{\mathrm{II}}\end{bmatrix}^{\mathrm{T}} \in \Re^{2+4N} \tag{25}$$

$$\mathbf{B_{rotor}} = \begin{bmatrix}B_{10}^{1,1}\cdots B_{6W_r}^{1,1}\cdots B_{10}^{1,2}\cdots B_{6W_r}^{K_r,L_r}\end{bmatrix}^{\mathrm{T}} \in \Re^{(2+4V_r)K_rL_r} \tag{26}$$

$$\mathbf{C_{stator}} = \begin{bmatrix}C_{10}^{1,1}\cdots C_{6W_s}^{1,1}\cdots C_{10}^{1,2}\cdots C_{6W_s}^{K_s,L_s}\end{bmatrix}^{\mathrm{T}} \in \Re^{(2+4V_s)K_sL_s} \tag{27}$$

$$\mathbf{U_1} = \begin{bmatrix}U^{1,1}\ U^{1,2}\ \cdots\ U^{1,L_{MEC}}\end{bmatrix}^{\mathrm{T}} \in \Re^{L_{MEC}} \tag{28}$$

$$\mathbf{U_2} = \begin{bmatrix}U^{2,1}\ U^{2,2}\ \cdots\ U^{2,L_{MEC}}\end{bmatrix}^{\mathrm{T}} \in \Re^{L_{MEC}}. \tag{29}$$

It should be noted that the total number of the unknown variables in (20) is

$$\begin{aligned}N_{\mathrm{tot}} = {} & 2\times(2+4N) + (K_rL_r)\times(2+4V_r)\\ & + (K_sL_s)\times(2+4V_s) + 2\times L_{MEC}.\end{aligned} \tag{30}$$

The choice of harmonic orders in the ESD regions can refer to [8]. The section number L_{MEC} of MEC regions should satisfy $L_{MEC} \geq 2N$ so that the Nyquist–Shannon sampling theorem holds for the relation between the spatial and the spatial harmonic mesh.

Furthermore, the last four lines of submatrices in (21) correspond to boundary conditions of the tangential magnetic field strength. They are dependent on the reluctivity of materials in the rotor and stator, and are related to the unknown variable vector $\mathbf{X}$. Then (20) can be rewritten as the following nonlinear system equations:

$$f(\mathbf{X}) = \mathbf{M}(\mathbf{X})\mathbf{X} - \mathbf{Y} = 0. \tag{31}$$

E. Modeling of Nonlinear Material

The magnetic reluctivity of material within each ESD of the stator and rotor is assumed to be a function of the mean value of magnetic field $\bar{B}$, which can be expressed using an analytical

description [19]

$$v(\bar{B}) = \frac{1}{\mu_0}\left[1 - \frac{Q}{\sum_{q=1}^{Q}((\bar{B}/m_q)^{n_q} + a_q^{n_q})^{1/n_q}}\right] \tag{32}$$

where μ_0 is the the vacuum permeability, q is an index, and m_q, n_q, a_q are the parameters to be optimized using genetic algorithm. For the slot and air-gap regions, the magnetic reluctivity is $1/\mu_0$.

Newton–Raphson technique is applied here to solve the nonlinear solution of (31)

$$\mathbf{X}^{k+1} = \mathbf{X}^k - (\mathbf{J}^k)^{-1} f(\mathbf{X}^k) \tag{33}$$

where $\mathbf{X}^k$ is the unknowns at kth iteration, $\mathbf{J}^k$ is the Jacobian matrix at kth iteration, which has been derived in [9].

F. Magnetic Force Calculation

After obtaining the magnetic flux density distribution in the air-gap, the magnetic force of AMB along the x and y directions can be predicted by the integral of Maxwell stress tensor based on the air-gap flux density, which is given by

$$F_x = L_z \int_0^{2\pi} \left[\frac{1}{2\mu_0}\left(B_r^{ag2} - B_\theta^{ag2}\right)\cos\theta - \frac{1}{\mu_0} B_r^{ag} B_\theta^{ag} \sin\theta\right] r d\theta \tag{34}$$

$$F_y = L_z \int_0^{2\pi} \left[\frac{1}{2\mu_0}\left(B_r^{ag2} - B_\theta^{ag2}\right)\sin\theta + \frac{1}{\mu_0} B_r^{ag} B_\theta^{ag} \cos\theta\right] r d\theta \tag{35}$$

where B_r^{ag} and B_θ^{ag} are the radial and tangential components of the flux density in the air-gap, respectively.

Consequently, the linearized current stiffness k_i and position stiffness k_s versus displacement and current of the AMB in the x and y directions can be derived from the magnetic force, given by

$$k_{i,pq} = \frac{\partial F_p}{\partial i_q} \tag{36}$$

$$k_{s,pq} = \frac{\partial F_p}{\partial e_q} \tag{37}$$

where subscripts p and q denotes x or y.

IV. Finite-Element Verification

The proposed model is validated by a 2-D nonlinear FEM, and the element statistics are given in Table III. For a tradeoff between accuracy and time consumption,the parameters used in the proposed model are taken as follows: $N = 200$, $V_r = W_r = 5$, $V_s = W_s = 20$, $K_r = 1$, $L_r = 8$, $K_s = 2$, $L_s = 16$, $L_{MEC} = 400$. The total number of the unknown variables of HAM are 5204.

A. Flux Density Validation

Figs. 5 to 7 present the comparison between the FEM results and HAM predictions for three cases in terms of the flux density distribution in different positions (marked by red dotted circles in Fig. 5(a). It can be seen that the HAM model results match well with the solutions of the FEM in the air-gap and rotor. However, the HAM results deviate slightly from the FEM results in the stator. This is because the stator tooth modeled by HAM is simplified by the assumption that stator tooth edges are along the radial direction whereas the FEM model is consistent with

TABLE III
FEM Element Statistics

Type	Number of elements
Triangles	9090
Edge elements	1125
Vertex elements	68
Average element quality: 0.8126	
Total number of degrees of freedom (DOF): 18213	

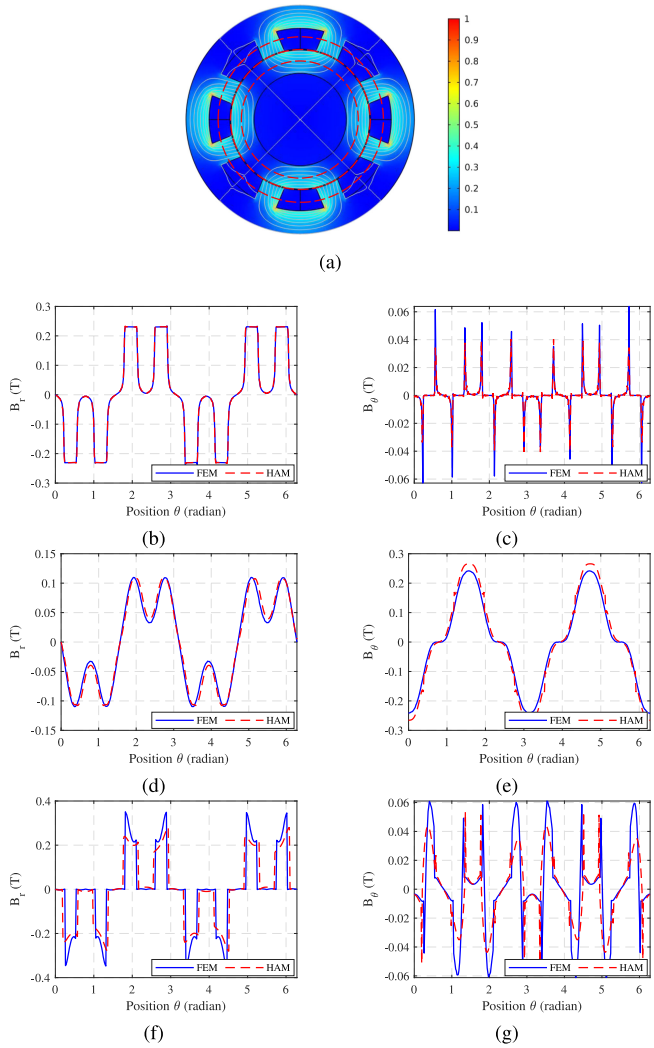

Fig. 5. (a) Magnetic flux density distribution in the AMB obtained by FEM without rotor eccentricity and equal currents in all windings. (b) and (c) Waveforms of B_r and B_θ in the middle of air-gap. (d) (e) Waveforms of B_r and B_θ in the middle of rotor yoke. (f) and (g) Waveforms of B_r and B_θ in the middle of stator teeth/slots.

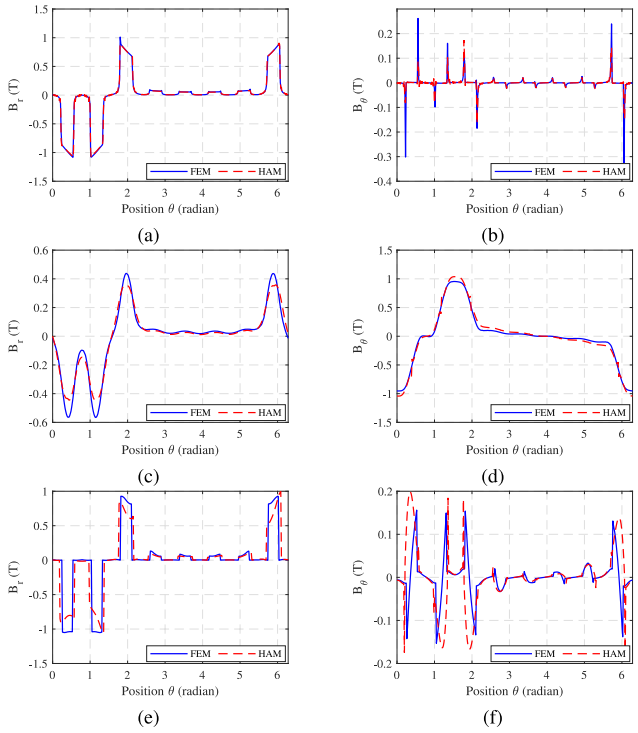

Fig. 6. Magnetic flux density distribution in the AMB with rotor eccentricity $\varepsilon = 0.2828$ mm, $\varphi = \pi/4$ and control currents $i_x = 3$ A, $i_y = 3$ A. (a) and (b) Waveforms of B_r and B_θ in the middle of air-gap. (c) and (d) Waveforms of B_r and B_θ in the middle of rotor yoke. (e) and (f) Waveforms of B_r and B_θ in the middle of stator teeth/slots.

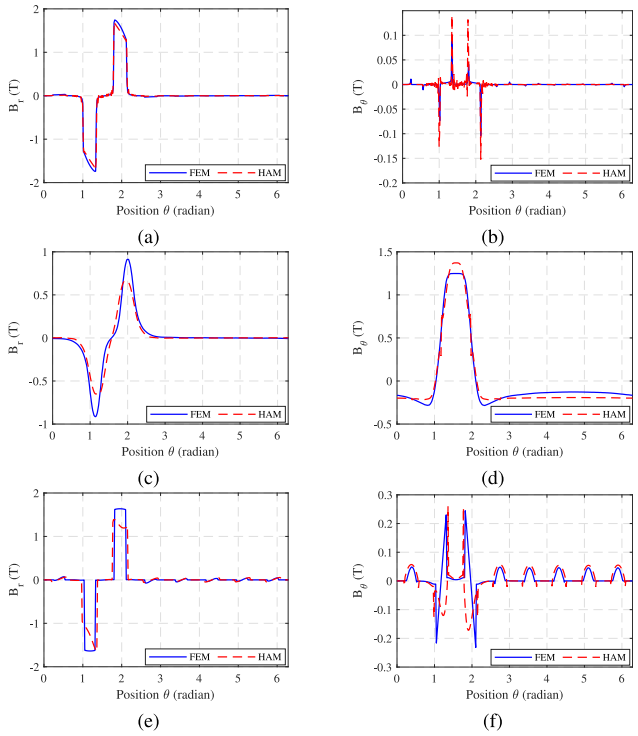

Fig. 7. Magnetic flux density distribution in the AMB with rotor eccentricity $\varepsilon = 0.35$ mm, $\varphi = \pi/2$ and control currents $i_x = 0$ A, $i_y = 3$ A. (a) and (b) Waveforms of B_r and B_θ in the middle of air-gap. (c) and (d) Waveforms of B_r and B_θ in the middle of rotor yoke. (e) and (f) Waveforms of B_r and B_θ in the middle of stator teeth/slots.

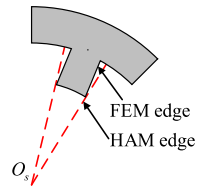

Fig. 8. Tooth model by FEM and HAM.

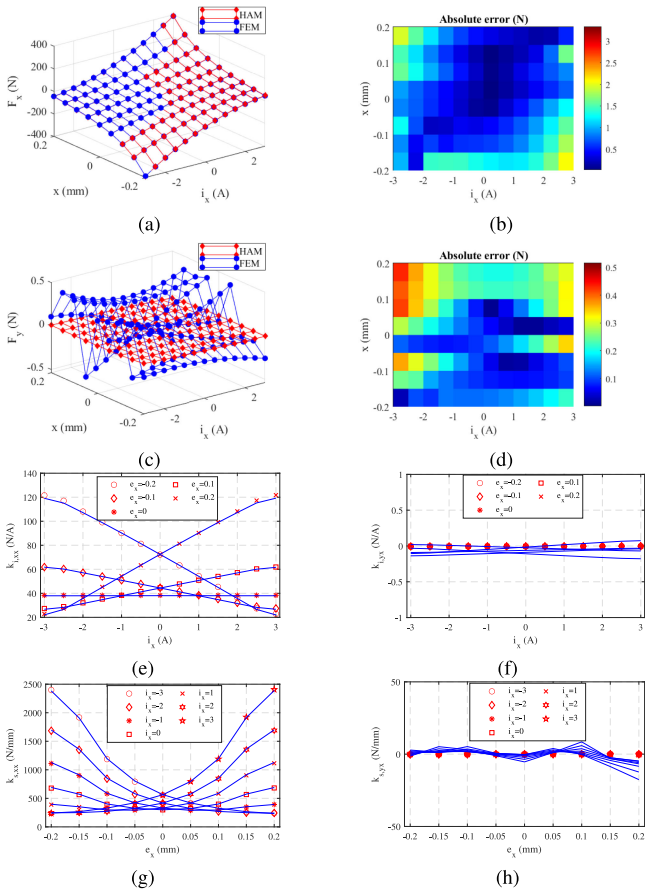

Fig. 9. Magnetic force and stiffness calculation results by HAM and FEM with $e_y = 0$ mm and $i_y = 0$ A. (a) and (b) Magnetic forces in x direction and absolute errors between HAM and FEM results. (c) and (d) Magnetic forces in y direction and absolute errors between HAM and FEM results. (e) and (f) Deduced current stiffness $k_{i,xx}$ and $k_{i,yx}$. (g) and (h) Deduced position stiffness $k_{s,xx}$ and $k_{s,yx}$ (blue indicates the results of FEM and red is for the results of HAM).

the actual case. The comparison is illustrated in Fig. 8. Such simplification does not affect the calculation of the air-gap flux density distribution and the magnetic forces according to the results.

B. Magnetic Force Validation

The magnetic force characteristic $F_x(i_x, i_y, e_x, e_y)$, position stiffness characteristic $k_s(i_x, i_y, e_x, e_y)$ and current gain characteristic $k_i(i_x, i_y, e_x, e_y)$ can be calculated over the entire operating range by the HAM model. Two cases of results by HAM and FEM in Figs. 9 and 10 are presented here. The difference between FEM and FEM in force calculations is quantified by

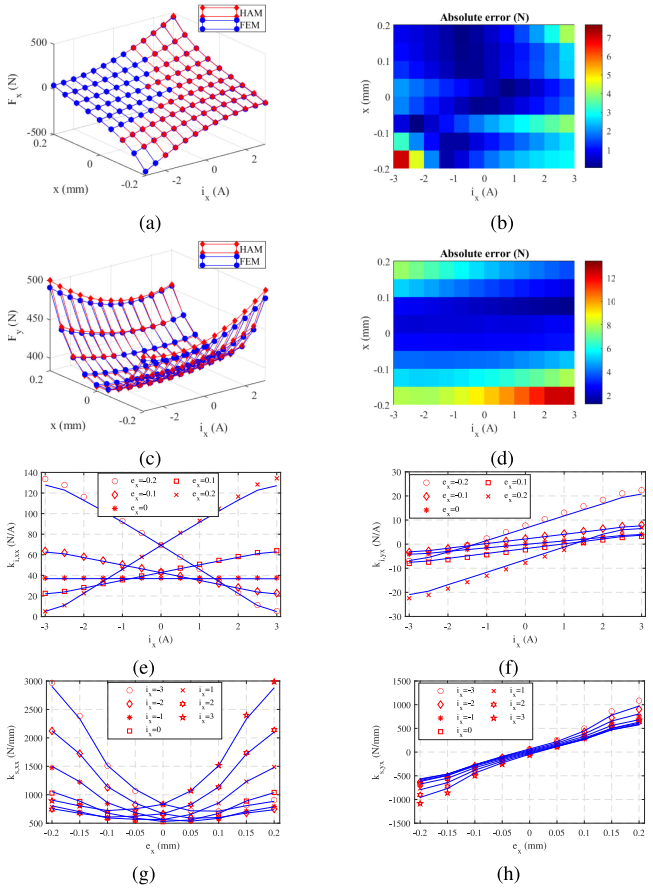

Fig. 10. Magnetic force and stiffness calculation results by HAM and FEM with $e_y = 0.2$ mm and $i_y = 3$ A. (a) and (b) Magnetic forces in x direction and absolute errors between HAM and FEM results. (c) and (d) Magnetic forces in y direction and absolute errors between HAM and FEM results. (e) and (f) Deduced current stiffness $k_{i,xx}$ and $k_{i,yx}$. (g) and (h) Deduced position stiffness $k_{s,xx}$ and $k_{s,yx}$ (blue indicates the results of FEM and red is for the results of HAM).

TABLE IV
ERRORS OF FORCE CALCULATION BETWEEN FEM AND HAM

Parameter	MAE (N)	MAPE (%)
Fig. 9b	0.8773	3.28
Fig. 9d	0.1797	98.42
Fig. 10b	1.6659	8.97
Fig. 10d	5.5583	1.30

mean absolute errors (MAE) and mean absolute percentage error (MAPE), and the results are depicted in Table IV. The errors stay at a low level except for the MAPE in Fig. 9(d) because the forces in Fig. 9(d) are quite close to zeros. The error increases slightly when the degree of saturation deepens and the eccentricity increases. The comparison shows a good agreement between FEM and HAM. Besides, it can be seen that the current gains and position stiffness vary according to the operating point. Moreover, coupling between x and y directions occurs when the rotor deviates from the center point in x or y axis, i.e., the coupling stiffness is nonzero. However, such coupling effects are always omitted during the simulation with a simplified AMB model [1], [2].

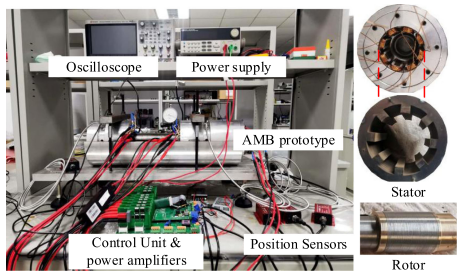

Fig. 11. AMB test setup.

C. Computation Time

The computation time of HAM for the concentric condition is around 0.9 s while that of FEM is about 3 s. The average computation time of HAM for eccentric conditions is 2.6 s while FEM requires an average of 10 s. Therefore, the proposed model is faster than FEM.

Furthermore, the computational complexity of HAM is given. The implementation of HAM contains four basic steps: 1) preparing the input data; 2) establishing the system equations; 3) solving the system equations; and 4) postprocessing.

The preparation of the input data mainly includes meshing in the ESD regions and MEC regions, and its complexity depends on the meshing element number N_e, i.e., $\mathcal{O}(N_\mathrm{e}) = \mathcal{O}(K_r L_r + K_s L_s + 2L_\mathrm{MEC})$. Then the complexity of forming the total matrix depends on the size of (21), namely, $\mathcal{O}(N_\mathrm{tot})$. Next, in each iteration of solving the system equations, the LU decomposition is used. The time complexity of each iteration is $\mathcal{O}(N_\mathrm{tot}^3)$. The postprocessing phase is mainly to predict the required quantities, which varies by the actual applications. This is a relatively simple task and its complexity is not considered here.

By adding all gained complexities, we obtain the generic expression of the complexity for the whole algorithm. Given that $N_\mathrm{tot} > N_\mathrm{e}$, the asymptotic complexity of the whole HAM algorithm is equal to

$$\mathcal{O}(N_\mathrm{e}) + \mathcal{O}(N_\mathrm{tot}) + \mathcal{O}(N_\mathrm{tot}^3) = \mathcal{O}(N_\mathrm{tot}^3). \tag{38}$$

V. EXPERIMENTAL VALIDATION

The AMB test setup and devices are shown in Fig. 11. To obtain the magnetic force in the experiment, a magnetic flux observer is designed according to [20] and the magnetic force can be deduced consequently. The rotor is actively controlled to the center position in the horizontal direction (i.e., $e_x = 0$ mm) and moved from bottom position to top in the vertical direction with a step pf 0.05 mm. When the current i_y changes from $-I_0$ to I_0, the magnetic forces in the y direction and the stiffness $k_{i,yy}, k_{s,yy}$ obtained in the experiment are shown in Fig. 12 and compared with analytical results and FEM. The deviation from the experiment results is calculated for FEM and HAM results and is listed in Table V. It can be seen that even at some extreme conditions where the iron part is saturated, the calculated forces by HAM agree well with the measured values. The comparison shows good agreements on force prediction between the HAM model and experimental results.

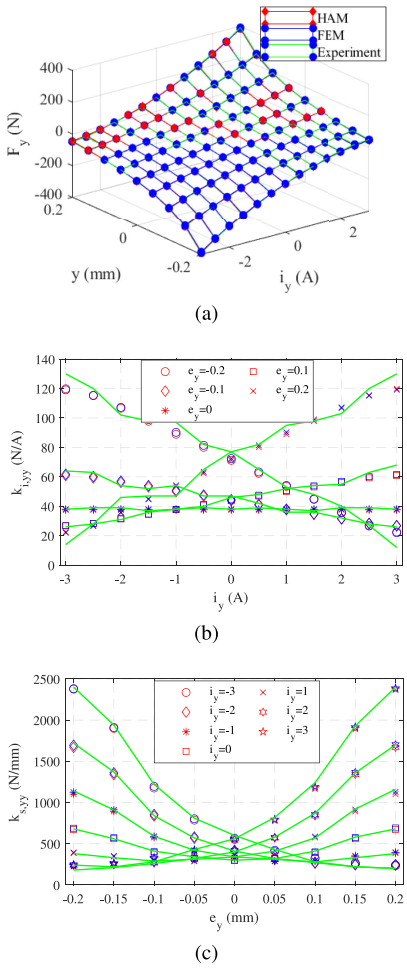

Fig. 12. Result comparison of the experiment, HAM and FEM under the condition of $e_x = 0$ mm and $i_x = 0$ A. (a) Magnetic forces F_y. (b) Current stiffness $k_{i,yy}$. (c) Position stiffness $k_{s,yy}$. (Blue indicates the results of FEM, red marker is for the results of HAM, and green is for the experimental results.)

TABLE V
FORCE ERRORS BETWEEN CALCULATED VALUES AND MEASURED VALUES

Parameter	MAE (N)	MAPE (%)
Experiment	-	-
FEM	1.458	5.3
HAM	2.2256	6.2

VI. CONCLUSION

This article presented an efficient HAM that integrates ESD and MEC to predict the AMB electromagnetic performance. It showed the capability to obtain accurate solutions over the entire operation range, i.e., with rotor eccentricity and saturation effects. This method was faster than FEM since the size of the HAM matrix was much smaller than that of FEM. In addition, force/stiffness calculations were straightforward and fast since the expression of the magnetic field in the air gap was obtained analytically. The HAM implemented in MATLAB could easily be integrated with algorithms for the optimization design and control simulation. Furthermore, the proposed HAM was easily applied to other electromagnetic actuators.

APPENDIX

Taking the boundary conditions at R_{g1} as an example, the elaborated expressions are derived as below. According to (1), (9), and (15), Fourier projection from MEC region to ESD region expands the expression of (18) as

$$\begin{aligned}
&-\frac{A_{20}^{\mathrm{I}(0)}}{\xi}\Big|_{\xi=R_{g1}} \\
&=\frac{1}{2\pi}\sum_{l=1}^{L_{MEC}}\int_{\theta_l-\frac{\Delta\theta}{2}}^{\theta_l+\frac{\Delta\theta}{2}} B_\theta^{1,l}\cos\left(\psi-\theta_l\right)d\psi \\
&-\frac{1}{2\pi}\sum_{l=1}^{L_{MEC}}\int_{\theta_l-\frac{\Delta\theta}{2}}^{\theta_l+\frac{\Delta\theta}{2}} B_r^{1,l}\sin\left(\psi-\theta_l\right)d\psi \qquad (39)\\
&-A_{1n}^{\mathrm{I}(0)}\frac{n}{\xi}\left(\frac{\xi}{R_g}\right)^n+A_{2n}^{\mathrm{I}(0)}\frac{n}{\xi}\left(\frac{R_r}{\xi}\right)^n\Big|_{\xi=R_{g1}} \\
&=\frac{1}{\pi}\sum_{l=1}^{L_{MEC}}\int_{\theta_l-\frac{\Delta\theta}{2}}^{\theta_l+\frac{\Delta\theta}{2}} B_\theta^{1,l}\cos(\psi-\theta_l)\sin\left(n\theta\right)d\theta \\
&-\frac{1}{\pi}\sum_{l=1}^{L_{MEC}}\int_{r_l-\frac{\Delta\theta}{2}}^{\theta_l+\frac{\Delta\theta}{2}} B_r^{1,l}\sin(\psi-\theta_l)\sin\left(n\theta\right)d\theta \qquad (40)\\
&-A_{3n}^{\mathrm{I}(0)}\frac{n}{\xi}\left(\frac{\xi}{R_g}\right)^n+A_{4n}^{\mathrm{I}(0)}\frac{n}{\xi}\left(\frac{R_r}{\xi}\right)^n\Big|_{\xi=R_{g1}} \\
&=\frac{1}{\pi}\sum_{l=1}^{L_{MEC}}\int_{\theta_l-\frac{\Delta\theta}{2}}^{\theta_l+\frac{\Delta\psi}{2}} B_\theta^{1,l}\cos(\psi-\theta_l)\cos\left(n\psi\right)d\theta \\
&-\frac{1}{\pi}\sum_{l=1}^{L_{MEC}}\int_{\theta_l-\frac{\Delta\theta}{2}}^{\theta_l+\frac{\Delta\psi}{2}} B_r^{1,l}\sin(\psi-\theta_l)\cos\left(n\psi\right)d\theta \qquad (41)
\end{aligned}$$

where θ_l is the center position angle of each MEC element center, which should be transformed to the corresponding value in the O_r–ξ–ψ coordinate system. It should be noticed that the flux density inside each MEC element is a constant.

Proceeding further, the boundary condition (19) can be elaborated by equaling the normal flux flowing into each MEC element at the interface from the ESD region, and combining (13), one can obtain

$$\begin{aligned}
&\left(A_z^{\mathrm{I}}\Big|_{\psi=\theta_l-\frac{\Delta\theta}{2}}^{\xi=R_{g1}}-A_z^{\mathrm{I}}\Big|_{\psi=\theta_l+\frac{\Delta\theta}{2}}^{\xi=R_{g1}}\right)L_z\cos\gamma \\
&-B_{\psi r}^{\mathrm{I}}\Big|_{\psi=\theta_l}^{\xi=R_{g1}}S_{rl}\sin\gamma-\phi_{rup}^{1,l}+\phi_{\theta l}^{1,l}-\phi_{\theta r}^{1,l}=0 \qquad (42)
\end{aligned}$$

with $\gamma=\arcsin(\frac{\varepsilon}{R_{g1}}\sin(\theta_l-\varphi))$ here.

REFERENCES

[1] G. Schweitzer and E. H. Maslen, *Magnetic Bearings: Theory, Design, and Application to Rotating Machinery*. Berlin, Germany: Springer-Verlag, Jun. 2009.

[2] T. Tezuka, N. Kurita, and T. Ishikawa, "Design and simulation of a five degrees of freedom active control magnetic levitated motor," *IEEE Trans. Magn.*, vol. 49, no. 5, pp. 2257–2262, May 2013.

[3] S. E. Mushi, Z. Lin, and P. E. Allaire, "Design, construction, and modeling of a flexible rotor active magnetic bearing test rig," *IEEE/ASME Trans. Mechatronics*, vol. 17, no. 6, pp. 1170–1182, Dec. 2012.
[4] J.-M. Jin, in *The Finite Element Method in Electromagnetics*, 3rd ed. New York, NY, USA: Wiley, Feb. 2015.
[5] F. Shakibapour, A. Rahideh, and M. Mardaneh, "2D analytical model for heteropolar active magnetic bearings considering eccentricity," *IET Electric Power Appl.*, vol. 12, no. 5, pp. 614–626, 2018.
[6] T. Du, H. Geng, Y. Zhang, H. Lin, Y. Li, and L. Yu, "Exact analytical method for active magnetic bearings with rotor eccentricity," *IEEE Trans. Magn.*, vol. 55, no. 12, pp. 1–12, Dec. 2019.
[7] F. Dubas and K. Boughrara, "New scientific contribution on the 2-D subdomain technique in polar coordinates: Taking into account of iron parts," *Math. Comput. Appl.*, vol. 22, no. 4, 2017, Art. no. 42.
[8] E. Devillers, "Electromagnetic subdomain modeling technique for the fast prediction of radial and circumferential stress harmonics in electrical machines," Ph.D. dissertation, Lab. Electr. Eng. Power Electron. (L2EP), Ecole Centrale de Lille, Villeneuve-d'Ascq, France, Dec. 2018.
[9] L. Roubache, K. Boughrara, F. Dubas, and R. Ibtiouen, "Elementary subdomain technique for magnetic field calculation in rotating electrical machines with local saturation effect," *COMPEL - Int. J. Comput. Math. Elect. Electronic Eng.*, vol. 38, no. 1, pp. 24–45, Jan. 2019.
[10] Y. X. Li and Z. Q. Zhu, "Cogging torque and unbalanced magnetic force prediction in pm machines with axial-varying eccentricity by superposition method," *IEEE Trans. Magn.*, vol. 53, no. 11, pp. 1–4, Nov. 2017.
[11] Y. Li, Q. Lu, Z. Q. Zhu, D. Wu, and G. Li, "Superposition method for cogging torque prediction in permanent magnet machines with rotor eccentricity," *IEEE Trans. Magn.*, vol. 52, no. 6, pp. 1–10, Jun. 2016.
[12] B. Guo, Y. Huang, F. Peng, J. N. Dong, and Y. Li, "Analytical modelling of misalignment in axial flux permanent magnet machine," *IEEE Trans. Ind. Electron.*, vol. 67, no. 6, pp. 4433–4443, Jun. 2020.
[13] B. Hannon, P. Sergeant, L. Dupre, and P. Pfister, "Two-dimensional fourier-based modeling of electric machines-an overview," *IEEE Trans. Magn.*, vol. 55, no. 10, pp. 1–17, Oct. 2019.
[14] J. Bao, B. L. J. Gysen, and E. A. Lomonova, "Hybrid analytical modeling of saturated linear and rotary electrical machines: Integration of fourier modeling and magnetic equivalent circuits," *IEEE Trans. Magn.*, vol. 54, no. 11, pp. 1–5, Nov. 2018.
[15] K. Pluk, "Hybrid 3-d electromagnetic modeling : The challenge of magnetic shielding of a planar actuator," Ph.D. dissertation, Dept. Electr. Eng., Technische Univ. Eindhoven, The Netherlands, Nov. 2015.
[16] U. Kim and D. K. Lieu, "Magnetic field calculation in permanent magnet motors with rotor eccentricity: Without slotting effect," *IEEE Trans. Magn.*, vol. 34, no. 4, pp. 2243–2252, Jul. 1998.
[17] L. Roubache, K. Boughrara, F. Dubas, and R. Ibtiouen, "New subdomain technique for electromagnetic performances calculation in radial-flux electrical machines considering finite soft-magnetic material permeability," *IEEE Trans. Magn.*, vol. 54, no. 4, pp. 1–15, Apr. 2018.
[18] J. Bao, S. R. Aleksandrov, B. L. J. Gysen, and E. A. Lomonova, "Analysis of variable flux reluctance machines using hybrid analytical modelling," in *Proc. 13th Int. Conf. Ecological Veh. Renewable Energies*, 2018, pp. 1–7.
[19] J. Cale, S. D. Sudhoff, and J. Turner, "An improved magnetic characterization method for highly permeable materials," *IEEE Trans. Magn.*, vol. 42, no. 8, pp. 1974–1981, Aug. 2006.
[20] C. M. Zingerli and J. W. Kolar, "Novel observer based force control for active magnetic bearings," in *Proc. Int. Power Electron. Conf.*, 2010, pp. 2189–2196.

Zhi Cao received the B.S. degree in electrical engineering in 2016 from Southeast University, Nanjing, China, where he is currently working toward the Doctor of Engineering degree in electric machines and control with the School of Electrical Engineering.

His main research interests include the design, analysis, and control of active magnetic bearing systems.

Yunkai Huang received the M.Sc. and Ph.D. degrees in electrical engineering from Southeast University, Nanjing, China, in 2001 and 2007, respectively.

He is currently a Professor with the School of Electrical Engineering, Southeast University and teaching "Electrical Machinery" and "Digital Signal Processing." His research interests include design and control of PM machine and high speed machine, applications in domestic appliances, electric vehicles, railway traction, all-electric ships, and wind power generation systems.

Baocheng Guo (Member, IEEE) received the B.E. degree from the China University of Petroleum, Qingdao, China, in 2009, the M.E. degree from the Harbin University of Science and Technology, Harbin, China, in 2014, and the Ph.D. degree from Southeast University, Nanjing, China, in 2017, all in electrical engineering.

He is currently an Assistant Professor with Nanjing Normal University, Nanjing, China, since 2020. Before joining NNU, he was a Postdoc Researcher with Southeast University. His research interests include the electromagnetic field computation and development of fast multiphysics models of electrical machines.

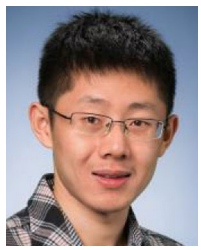

Fei Peng (Member, IEEE) received the B.S. and M.S. degrees in electrical engineering from Southeast University, Nanjing, China, in 2010 and 2012, respectively, and the Ph.D. degree in electrical and computer engineering from McMaster University, Hamilton, ON, Canada, in 2016.

After that he was a Postdoctoral Fellow with the McMaster Institute for Automotive Research and Technology, McMaster University. In December 2016, he joined the School of Electrical Engineering, Southeast University as an Assistant Professor. His research interests include optimal design and control of power converters, modeling, and digital control of motor drives.

Jianning Dong (Member, IEEE) received the B.S. and Ph.D. degrees in electrical engineering from Southeast University, Nanjing, China, in 2010 and 2015, respectively.

Since 2016, he has been an Assistant Professor with the Delft University of Technology (TU Delft), Delft, the Netherlands and is teaching "Electromechanics." Before joining TU Delft, he was a Postdoctoral Researcher with McMaster Automotive Resource Centre, McMaster University, Hamilton, ON, Canada. His main research interests include design, modeling, and control of electromechanical systems.

Ahmed Hemeida received the B.Sc. and M.Sc. degrees in electrical engineering from the Department of Electrical Power and Engineering, Cairo University, Giza, Egypt, in 2009 and 2012, respectively, and the Ph.D. degree from the Department of Electrical Energy, Metals, Mechanical Constructions and Systems, Ghent University, Ghent, Belgium.

He worked afterward as a Postdoctoral Research Assistant with the Department of Electrical Engineering, Aalto University, Espoo, Finland. He is currently working as an Assistant Professor with the Electrical Engineering Department, Cairo University. His research interests include the modeling, control, and design of electrical machines.